On the Creation, Depletion, and End of Life of Polar Cap Patches

Nina Kristine Eriksen[1,2], **Dag A. Lorentzen[1,2]**, **Kjellmar Oksavik[1,2]**, **Lisa Baddeley[1,2]**, **Keisuke Hosokawa[3]**, **Kazuo Shiokawa[4]**, **Emma Bland[1]**, **Larry Paxton[5]**, **Yongliang Zhang[5]**, **Kathryn McWilliams[6]**, **Tim Yeoman[7]**, and **David R. Themens[8,9]**

[1]Department of Arctic Geophysics, The University Centre in Svalbard, Longyearbyen, Norway, [2]Department of Physics and Technology, Birkeland Centre for Space Science, University of Bergen, Bergen, Norway, [3]Department of Communication Engineering and Informatics, University of Electro-Communications, Tokyo, Japan, [4]Institute for Space-Earth Environmental Research, Nagoya University Furo-cho, Nagoya, Japan, [5]The Johns Hopkins University Applied Physics Laboratory, Laurel, MD, USA, [6]Department of Physics and Engineering Physics, University of Saskatchewan, Saskatoon, Saskatchewan, Canada, [7]University of Leicester, School of Physics and Astronomy, Leicester, UK, [8]Space Environment and Radio Engineering (SERENE) Group, University of Birmingham, Birmingham, UK, [9]Department of Physics, University of New Brunswick, Fredericton, York, Canada

Abstract Ionospheric convection patterns from the Super Dual Auroral Radar Network are used to determine the trajectories, transit times, and decay rates of three polar cap patches from their creation in the dayside polar cap ionosphere to their end of life on the nightside. The first two polar cap patches were created within 12 min of each other and traveled through the dayside convection throat, before entering the nightside auroral oval after 104 and 92 min, respectively. When the patches approached the nightside auroral oval, an intensification in the poleward auroral boundary occurred close to their exit point, followed by a decrease in the transit velocity. The last patch (patch 3) decayed completely within the polar cap and had a lifetime of only 78 min. After a change in drift direction, patch 3 had a radar backscatter power half-life of 4.23 min, which reduced to 1.80 min after a stagnation, indicating a variable decay rate. 28 minutes after the change in direction, and 16 min after coming to a halt within the Clyde River radar field-of-view, patch 3 appeared to reach its end of life. We relate this rapid decay to increased frictional heating, which speeds up the recombination rate. Therefore, we suggest that the slowed patch motion within the polar cap convection pattern is a major factor in determining whether the patch survives as a recognizable density enhancement by the time the flux tubes comprising the initial patch cross into the nightside auroral oval.

1. Introduction

Polar cap patches (PCPs) are isolated, dense segments in the F-region of the ionosphere with enhanced plasma densities at least twice that of the ambient plasma (Carlson, 2012; Crowley, 1996; Weber et al., 1984). The plasma source of the PCPs often comes from dayside subauroral latitudes where a reservoir of enhanced plasma is produced by photoionization from solar EUV radiation. However, particle precipitation in the cusp and polar cap can also contribute to patch formation (Goodwin et al., 2015; Lockwood et al., 2005; Oksavik et al., 2006; Rodger et al., 1994; Walker et al., 1999). The study of the complete transit of PCPs from their creation to their end of life is often a complicated process due to scarce data coverage. PCPs travel with the convection velocity, however this flow is often turbulent at the meso-scale level and the influence on the PCP structure and transit path across the polar cap is still under discussion. The optical signature of PCPs is known as airglow patches, which often occur after the optical signature of pulsed reconnection, namely poleward moving auroral forms (PMAFs) (Sandholt et al., 1986, 1998, 2004; Southwood, 1987). Airglow patches are mainly seen as 630.0 nm airglow emissions (as opposed to 630.0 nm auroral emissions) since the light stems from de-excitation of atomic oxygen around 250 km altitude (Hays et al., 1978):

$$O^*(^1D) \rightarrow O(^3P) + h\upsilon_{630.0nm} \tag{1}$$

However, the intensity stemming from the 630.0 nm emission line can be dependent on changes in altitude of the bottom of the plasma layer (Valladares et al., 2015), which again would influence the recombination rates to the neutrals in the atmosphere.

There are several case studies of airglow patches (Hosokawa et al., 2009, 2016; Perry et al., 2013; Weber et al., 1984; Zou et al., 2015), but only a few reports have corresponding electron density measurements (cf. Lorentzen et al., 2010; Pedersen et al., 2000). Recent studies that have successfully followed patches for most of their lifetime across the polar cap are Oksavik et al. (2010), Q. H. Zhang et al. (2013), Nishimura et al. (2014), Spicher et al. (2015), Thomas et al. (2015), Q. H. Zhang et al. (2016), and Hwang et al. (2020).

Oksavik et al. (2010) used the EISCAT Svalbard Radar (ESR) (Wannberg et al., 1997) and the Super Dual Auroral Network (SuperDARN) (Chisham et al., 2007; Greenwald et al., 1995; Nishitani et al., 2019) to study the transit of two extreme electron density events ($n_e > 10^{12}\mathrm{m}^{-3}$). They found that the two events underwent a substantial rotation as they crossed the polar cap and were observed to have pulsed flow speeds. Nishimura et al. (2014) conducted a study of patch propagation across the polar cap using SuperDARN and all-sky camera measurements and reported a PMAF which evolved into a polar cap airglow patch on the dayside. They followed the airglow patch through optical measurements and observed a fast flow channel coincident with the airglow patch through polar boundary intensification and localized reconnection on the nightside.

Although SuperDARN measurements and other instruments have previously been able to track PCPs for their entire lifetime, there is still a need for a more generalized tracking method that is not solely dependent on extreme events or optimal observation alignment. PCPs are considered a space weather challenge (Jin et al., 2014; Moen et al., 2013; Oksavik et al., 2015; Van Der Meeren et al., 2014), due to their ability to disrupt transionospheric radio frequency signals, which can be detrimental at polar latitude. Therefore, a robust tracking method would be an important application for forecasting PCP trajectories. In addition, successful tracking of PCPs allows us to study changes to their morphology by uniting observations at various stages of their lifetime. The electron density decay rate throughout a patch's lifetime is still up for debate. Only a few studies have addressed the electron density decay rate of PCPs or small-scale plasma structures (∼1 km) in the F-region (Hosokawa et al., 2011; Ivarsen et al., 2021).

This paper presents several PCPs detected by the ESR (78.15°N, 16.1°E) on 19 December 2014. We follow three patches across the polar cap. Their trajectories are determined from SuperDARN convection maps and confirmed optically by measurements of airglow patches seen over Ny Ålesund (78.92°N, 11.93°E) and Resolute Bay (74.73°N, 265.07°E), as well as backscatter echoes from individual SuperDARN radars from Hankasalmi, Clyde River, Rankin Inlet, and Inuvik. Two of the patches transited the entire polar cap and entered the auroral oval near magnetic midnight. The third patch rotated after passing the magnetic pole and did not exit the polar cap before becoming indistinguishable from the ambient plasma in the nightside dawn convection cell.

2. Instrumentation and Data Presentation

2.1. Solar Wind and Magnetic Data

The NASA Advanced Composition Explorer satellite (ACE) was located at the L1 Lagrangian point and provides data for the solar wind and interplanetary magnetic field (IMF) conditions. In Figures 1a and 1b the IMF components and the clock angle measurements are given for the period 06:30 to 09:30 UT, respectively. On 19 December 2014 we observe a generally steady and strong positive IMF By, together with a positive clock angle around 100°, as well as some changes in the north-south IMF direction. The solar wind velocity was steady around 350–400 km/s, and the proton density was, for the most part, around 3.6 cm^{-3}, with a single spike above 8 cm^{-3} at 08:10 UT (data not shown). The solar wind data are presented in Figures 1a and 1b, with a 70-min time shift from L1 to the dayside ionosphere, which was found using mean solar wind velocity and dayside aurora activity. The relevant time period on 19 December 2014 had no geomagnetic storm activity with SYM-H > −25 nT and a Kp-index between 1 and 2.

The Defense Meteorological Satellite Program (DMSP) SSUSI LHBS auroral image (Paxton et al., 2002; Paxton & Meng, 1999; Paxton & Zhang, 2016) and SSIES Horizontal ion velocity is presented in Figure 2a). The data is from the F16 pass as the satellite was crossing the polar cap. It passed over Svalbard between 06:52 and 06:54 UT. The data provides a large-scale context of the auroral oval and the ionospheric flow immediately prior to the time of interest in this paper. The figure shows that Svalbard (78°N, 16°E geographic) is located within the polar cap due to the expanded oval, with an antisunward flow direction in the pre-noon polar cap, which is consistent with positive IMF By.
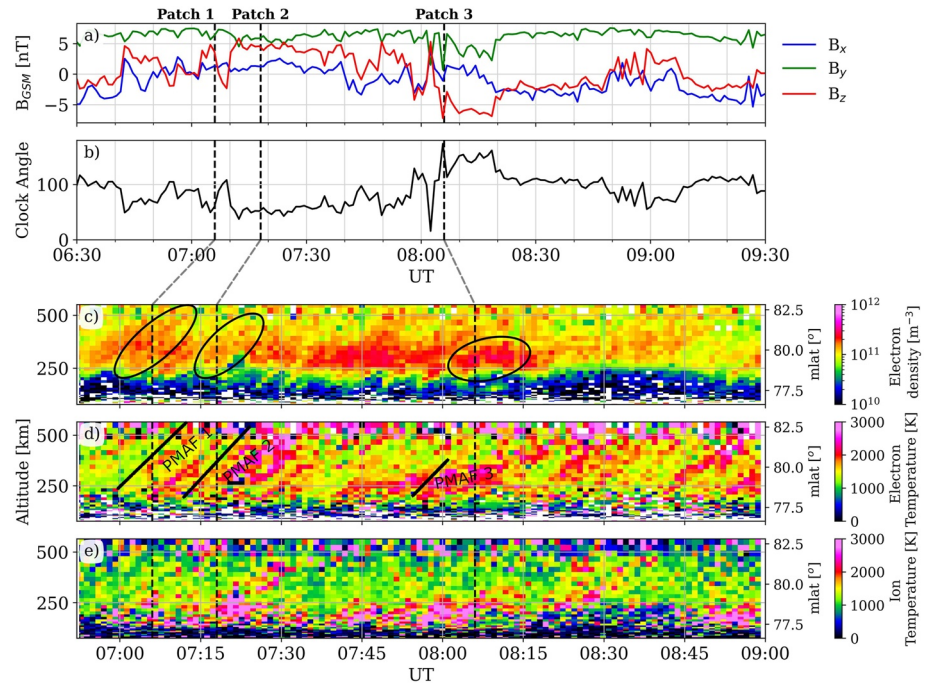
Figure 1. (a) Interplanetary magnetic field measurements from ACE and (b) shows corresponding clock angles on 19 December 2014. (c) shows ESR 32m electron number density, and (d) and (e) show ESR 32m electron and ion temperatures, respectively. ESR measured at 30° elevation during this time period. Release times for patches 1, 2, and 3 are seen as vertical, dashed lines and their density signatures are circled. The PMAFs are labeled, and their start time is represented by a black, tilted line.
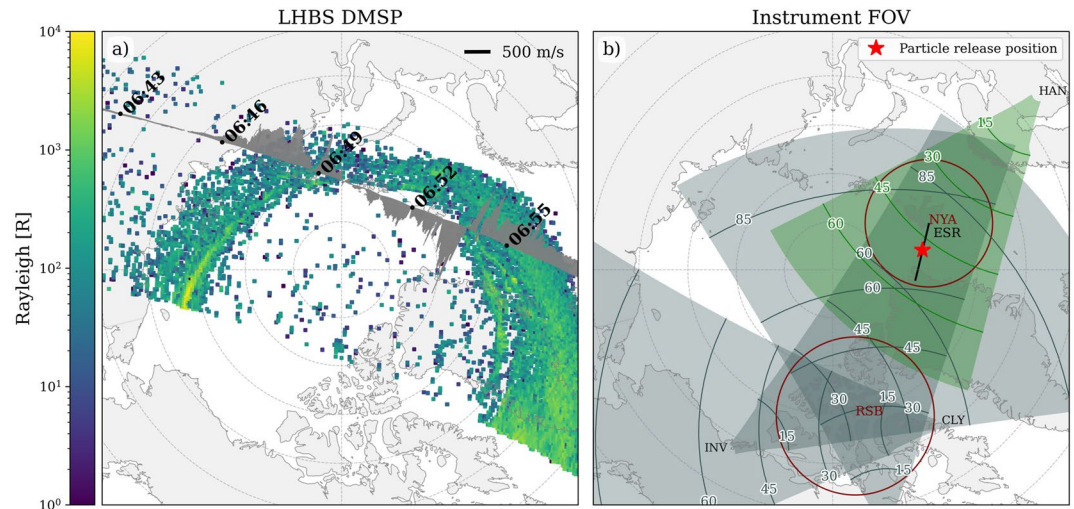
Figure 2. (a) Measurements of the auroral oval from DMSP SSUSI auroral data (LHBS) and SSIES horizontal ion velocity at 06:43–06:59 UT in geographical coordinates. (b) Field-of-view of the individual SuperDARN radars: Hankasalmi (HAN) is shown in green, and Inuvik (INV), Rankin Inlet (RKN) and Clyde River (CLY) are shown in gray. The field-of-view of the two all-sky imagers located at Ny Ålesund (NYA) and Resolute Bay (RSB) are seen as maroon circles. The location of the 32 m EISCAT Svalbard Radar beam is shown as a black line. The location where the particles were released for tracking across the polar cap is marked with a red star. The locations are all given in geographical coordinates.

2.2. European Incoherent Scatter Svalbard Radar

The ESR steerable 32m dish was measuring at a low elevation of 30° and an azimuth direction of 331° (where 0° is at geographic north) on 19 December 2014. The radar provided measurements of the ionospheric parameters; electron density, electron temperature and ion temperature, presented in Figures 1c–1e, respectively. The field-of-view (FOV) of the radar is presented as a solid black line in Figure 2b. In addition, Figures 1c and 1d show the density signatures of the three patches and the respective PMAF-temperature enhancement, outlined in black. The differences between the patch signatures are discussed in Section 5.

2.3. All-Sky Imagers: 630.0 nm Emission

The optical measurements presented in this study are provided from two all-sky imagers (ASIs) equipped with 630.0 nm narrow bandpass interference filters. The ASI located in Ny Ålesund (NYA) is owned by the University of Oslo (UiO) and provides images mapped to 250 km altitude for elevation angles above 19°. Images from the Resolute Bay Optical Mesosphere Thermosphere Imagers ASI (RSB) are mapped to 230 km altitude with measurements above 20° elevation angles (Shiokawa et al., 1999, 2009). The mapping altitudes correspond to the expected altitudes for de-excitation of atomic oxygen, and thus airglow emissions. Both camera FOVs are presented in Figure 2b as maroon circles.

When considering airglow patch location and size, the background is removed using a 1-hr running average in order to focus on weaker perturbations in the airglow intensity. The images are subsequently converted to relative intensity using the same one-hour running average. Finally, they are presented as a percentage relative to a background intensity:

$$100 \cdot (I_{measured} - I_{backgr})/I_{backgr} \tag{2}$$

where I_{backgr} is the one-hour running average representing the background intensity.

However, for the intensities obtained in each trajectory step, uncorrected images (emission intensities) are used. These measurements are influenced by background emissions, atmospheric absorption, instrumental effects—and when obtained at low elevation—the van Rhijn effect (van Rhijn, 1919).

2.4. Super Dual Auroral Radar Network

Ionospheric convection patterns determined from the SuperDARN radars were used to estimate the trajectories of the three patches over the polar cap. The convection patterns were determined using the SuperDARN Radar Software Toolkit (RST) (SuperDARN Data Analysis Working Group et al., 2021). The data had been processed from the raw radar data using the standard SuperDARN fitting algorithm called FitACF3.0 to estimate the line-of-sight (LOS) velocity parameter. Additional tools in the RST were then used to combine the IMF data provided in Section 2.1 and data from all northern hemisphere radars onto a grid of equal-area cells spanning 1° of magnetic latitude, and then determine the convection pattern using the standard SuperDARN "Map Potential" algorithm (Ruohoniemi & Baker, 1998).

In addition to the northern hemisphere convection patterns, backscatter power and LOS velocity measurements from the SuperDARN radars at Hankasalmi, Inuvik, Rankin Inlet and Clyde River were used to identify and track the PCPs at various locations in the polar cap. The FOV of these radars are shown in Figure 2b. These data were also processed using the FitACF3.0 fitting algorithm in the RST.

3. PCP Tracking Method

3.1. Virtual Particle Tracking With SuperDARN Data

A simple particle tracking method was developed using a geomagnetic (MLAT, MLON) reference system. Given the initial release coordinates, the SuperDARN convection maps were used to calculate the subsequent particle location using the velocity vectors. A particle at position a with speed v_a and azimuth angle k_a was used to give the next latitude and longitude coordinates at position b through the Haversine formula for great-circle distance. The process was repeated for 4 hr with a time cadence of 2 min. Repeatedly releasing particles every 2 minutes between 06:50 and 08:30 UT, which correspond to the period of higher density seen in Figure 1c, allowed us to determine release times for the three PCP events.

The initial release location in geographical coordinates was 80.42°N and −1.64°E, corresponding to the ESR beam at 281 km altitude. The release altitude was chosen close to the median altitude for the electron density peak

in the F-region between 06:00 and 12:00 UT and based on the best fit between the virtual particle trajectories and the observed airglow patches. Choosing a different initial release location could lead to a clear difference in the resulting trajectories as flow shears could send the particles into different directions.

3.2. Event Selection

The three PCP events were selected based on: (a) ESR measurement of high density in F-region and no significant temperature enhancements, that is, temperature enhancement not related to the PMAF, (b) patch production/source features in the vicinity on the dayside, that is, PMAFs or tongue of ionization (TOI) (cf. Foster et al., 2005) as observed by the UiO ASI and TEC measurements from satellites (not shown), (c) simultaneous observations of airglow patch movement, and (d) simultaneous observations of strong backscatter power in the individual SuperDARN radars, preferable Clyde River and Inuvik due to their favorable FOV orientation.

4. Results

Using all four selection criteria outlined in the above section, three trajectories were chosen patch 1 (P1), patch 2 (P1), and patch 3 (P3). From Figure 1c P1 and P2 have lower electron densities than P3 and appear more isolated. The low elevation angle of the ESR means that a poleward motion of the patches (along the look direction of the radar beam) manifests itself as an apparent altitude increase as a function of time, resulting in the "slanted" shape of the structures. P3 has a higher electron density and stems from a time with more continuous, high-density plasma passing over the ESR. The measurements indicate that the patches originate from the TOI; denser Solar-EUV ionospheric plasma transported from lower latitudes into the polar cap. There are no significant temperature increases, outside of those related to the PMAFs, seen in the ESR for the three patches, suggesting high density isolated volumes that migrate into the polar cap. TEC maps show high density and high phase scintillation, indicating dense, structured plasma in the F-region (not shown).

4.1. Multimedia Material

This paper is accompanied by two videos, one embedded and one supplementary. It is strongly encouraged to watch Video 1 before reading the rest of the paper, as this video provides a dynamical presentation of the airglow patches, the auroral oval and the motion of the selected events. Video 1 presents virtual particles released every second minute between 06:50 and 08:30 UT and their geographic locations in the polar cap. The selected events are presented as blue stars, the remaining virtual particles as gray dots. Corresponding ASI 630.0 nm images from NYA and RSB are included. In addition, ASI images from Fort Smith and Fort Simpson, which are both equipped with 557.7 nm narrow bandpass interference filters, from the history of events and macroscale interactions during substorms (THEMIS) network were included in Video 1 to investigate potential auroral interactions in the nightside auroral boundary as the PCPs traversed the nightside polar cap. Also included, when available, are the DMSP SSUSI modeled poleward and equatorward auroral boundaries, shown in coral, to provide a proxy for the auroral oval (Y. Zhang & Paxton, 2008). The satellite number and swath time is presented at the bottom of each frame.

The airglow patches were identified using Video 1 and uncorrected ASI images from NYA and RSB (not shown). In Video 1, weak airglow patches corresponding to P1 and P2 can be seen at the north-western edge of the NYA FOV after the corresponding PMAF has retreated. Next, the airglow patches enter the north-eastern RSB FOV. As the airglow patches move toward the FOV center high-intensity, small-scale arc-like structures can be seen embedded within the patches. P3's airglow patch also exits the north-western edge of the NYA FOV, before it appears in the north-eastern RSB FOV.

Video S1 (Supporting Information S1) presents the location of P1, P2, and P3 (red stars) as they transit the polar cap in the geomagnetic reference frame. The convection velocity maps, seen as the underlaying color-map, from SuperDARN RST processing are included to provide information on the ionospheric convection. The video does not include the LOS velocities for the northern hemisphere, but instead includes the fitted vector velocities, seen as dots with respective vector lines. Also seen, in coral, are the DMSP SSUSI auroral boundaries. Going forth, data from convection velocity maps are referred to as convection model velocity, model velocity or Px velocity.

4.2. Patch 1 & 2: Release Times at 07:06 & 07:18 UT

Because P1 and P2 show many similarities they will be presented together. In Video 1 an intensification in the aurora on the dayside can be seen at 06:58 UT, followed by a PMAF that disappears at 07:16 UT. At 07:06 UT the virtual
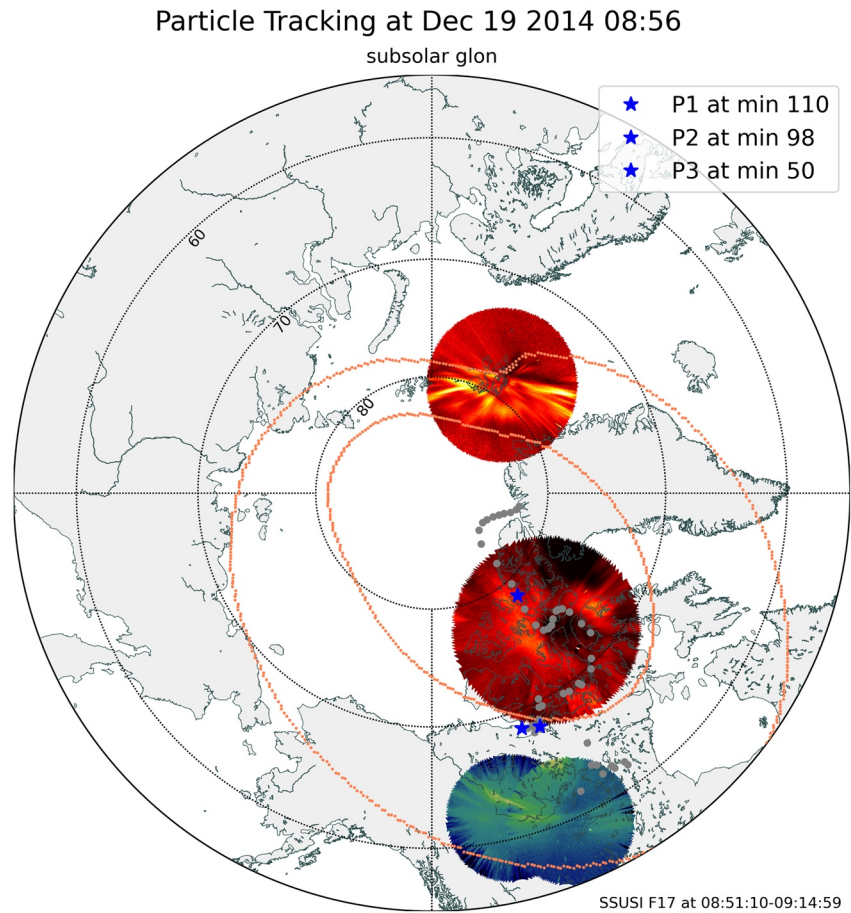
Video 1. Shows the tracking of the virtual particles released between 06:50 and 08:30 UT in geographical coordinates. The selected events are shown as blue stars and the remaining as gray dots. The DMSP SSUSI auroral boundaries are shown in coral. All-sky images (630.0 nm filtered) from Ny Ålesund and Resolute Bay, as well as images from Fort Smith and Fort Simpson (557.7 nm filtered) are also included. The placeholder image is from 31 s into the video.

particle was released representing P1. P2 was released during a PMAF, which started with an intensification at 07:12 UT and moved poleward until 07:36 UT. Figure 1c shows an elevated electron density during both release times.

Both P1 and P2 move across the polar cap within the convection throat (See Video S1 in Supporting Information S1), and their trajectories are presented in Figure 3a. DMSP SSUSI auroral boundaries, auroral oval activity seen in 557.7 nm filtered ASI images from Fort Smith and Fort Simpson indicate that P1 and P2 have already entered the nightside auroral oval at minute 104 and 92 (08:50 UT), respectively. From minute 94 and 82 (08:40 UT) for P1 and P2, respectively, intensifications in the nightside auroral oval can be seen in Video 1. The intensifications occur several times until the end of both patches' lifetime. It is worth noting that the two patches arrived at the nightside auroral boundary in close proximity, suggesting a nonlinearity in the convection pattern. This will be discussed in more detail in Section 5.1.

In Figure 4a we present the P1 velocity determined from the convection pattern as it transits the polar cap, seen as a line. The markers show the LOS velocity measurements, in a geocentric reference frame, of individual radars within 100 km of P1. Panel b) presents the uncorrected intensity of the NYA and RSB cameras. The intensity was collected at the position of P1, given that the measurements elevation angle was larger than 20°. Figures 4c–4e show uncorrected ASI images from NYA and RSB for different minutes in the P1 trajectory. Figure 4c shows the location of P1 at minute six in the newly created airglow patch after the PMAF has disappeared. Figures 4d and 4e show the airglow patch recently entering and close to leaving the RSB FOV at minute 56 and 86, respectively.

Figure 4a show a variable velocity ranging from below 300 m/s to almost 750 m/s. A decrease in velocity close to the end of life of P1 at minute 96 coincides with the intensifications seen in the nightside auroral oval. In panel
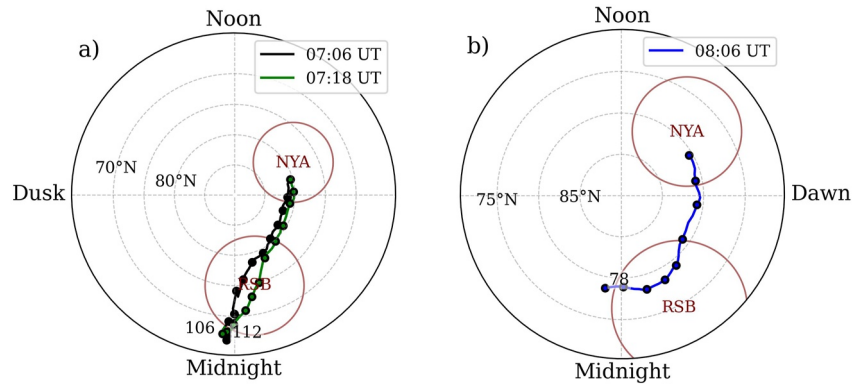
Figure 3. (a) and (b) show the trajectories of the virtual particles released at 07:06 and 07:18 UT, and 08:06 UT respectively. Each tenth minute of the trajectories, in addition to the first and final minutes, are marked as black rings. The Ny Ålesund (NYA) and Resolute Bay (RSB) camera FOVs are shown in maroon.

(b) a rapid decrease in intensity, related to the PMAF emission and decreasing elevation angles, is seen as P1 moves in the NYA FOV. In the RSB FOV a steadier intensity is seen, with some slight increases in the edges of the FOV, which is related to the aurora activity in the night side oval. In Video 1 small, arc-like structures, can be seen between minute 32 and 88 (07:38 and 08:34 UT) in the RSB FOV. These structures, although less prominent, are also presented in Figures 4d and 4e. Since the ASI measures both aurora and airglow, the airglow decay rate of P1 could include a contribution from aurora for example, from small-scale auroral-arcs.
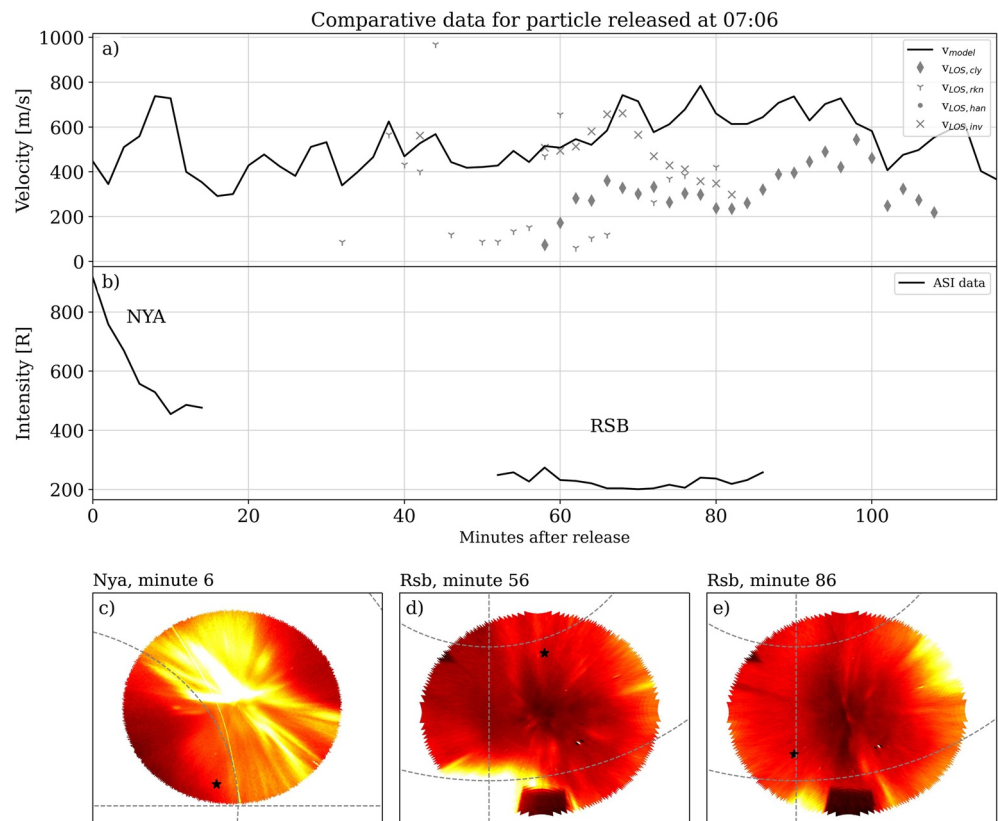
Figure 4. Results for patch 1, released at 07:06 UT, during its trajectory across the polar cap. Panel (a) shows the convection velocity at each step in the transit and the individual radar LOS velocities that were within 100 km of the virtual particle position. Panel (b) shows the uncorrected emission intensity at the particle's position, when available. (c) Shows a Ny Ålesund ASI image at minute 6 of the trajectory, and (d)–(e) show Resolute Bay ASI images at minutes 56 and 86, respectively. The star represents the tracking location at the time. The orientation of the cameras is shown in Figure 3a.

Figure 5. Same format as Figure 4, but for patch 2 released at 07:18 UT.

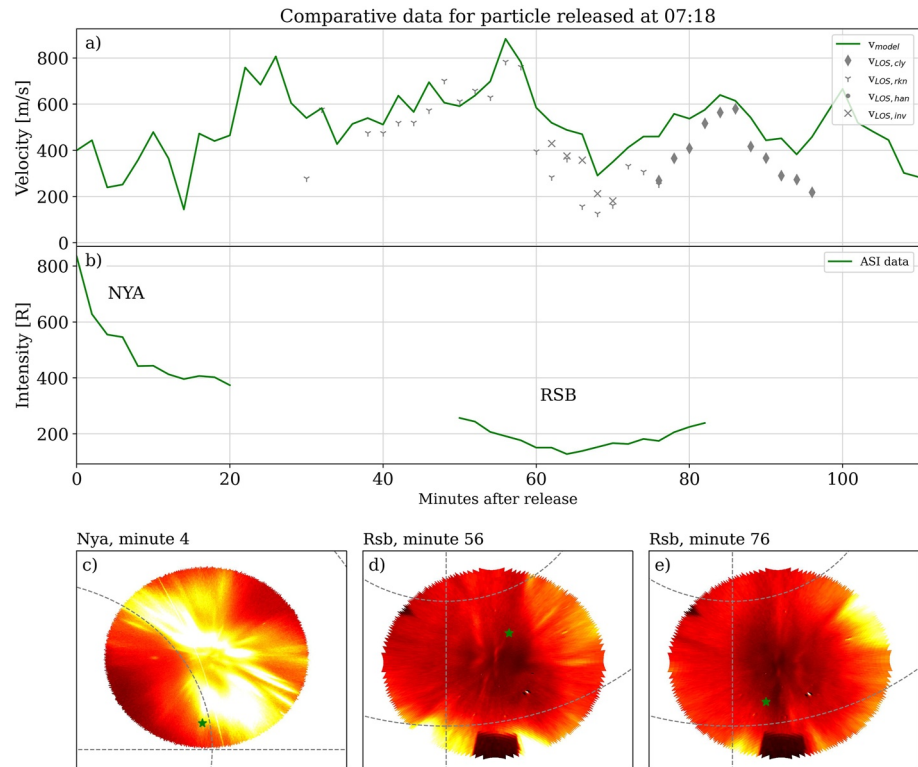P2 shows a more variable and pulsed velocity compared to P1, varying from around 144 m/s to around 880 m/s during the transit, see Figure 5a. Like P1, the decrease in velocity seen at minute 84 coincides with the intensities seen in the nightside auroral oval. Similar to P1, there is a decrease in the intensity as P2 is within the NYA camera FOV. Within the RSB camera FOV, P2 experiences a minimum in the intensity close to zenith. In Figures 5c–5e we present ASI images from NYA and RSB during minute 4, 56, and 76, respectively. In panel (c) P2 is still within the PMAF it was released into, and in panel (d) and (e) we can see the small-scale aurora arc-like structures embedded within the airglow patch.

4.3. Patch 3: Release Time at 08:06 UT

Video 1 shows high activity, and a brightening of the dayside auroral oval at 07:50 UT, followed by a PMAF observed until 08:12 UT. However, the PMAF seems to be more intense with a brightening moving westward in the camera FOV, instead of a typical initial brightening at the equatorward boundary as seen for P1 and P2. Figure 3b shows that there is a change in the direction of motion of P3. Initially, P3 moves within the convection throat, before a rotation occurs around minute 50. Afterward, P3 drifts toward dusk and does not appear to leave the polar cap.

In Figure 6a the P3 velocity increases till it reaches a maximum of over 1,000 m/s at minute 28, and for the remainder of the trajectory the velocity generally vary between 400 and 600 m/s. Between minute 52 and 78, the LOS velocities measured by Clyde River radar are very close to the model velocities. This suggests that P3 was moving parallel to the radar beam during this time. Figure 6b shows a decrease in emission intensity from minute 50 to 60 after a period of high intensity, which appears to correspond to the second velocity increase seen in panel (a). In Video 1 there is no indication of auroras as the airglow patch corresponding to P3 moves within the RSB FOV. This can be seen in Figures 6d and 6e, which shows the airglow patch at the intensity maximum at minute 42 and a dimmer airglow patch at minute 58.

Figures 7a and 7b show the radar backscatter power and LOS velocity, respectively, as P3 travels along Clyde River beam 14 as it nears its end of life. Figures 7c–7k show the movement of P3 (outlined in green, which was
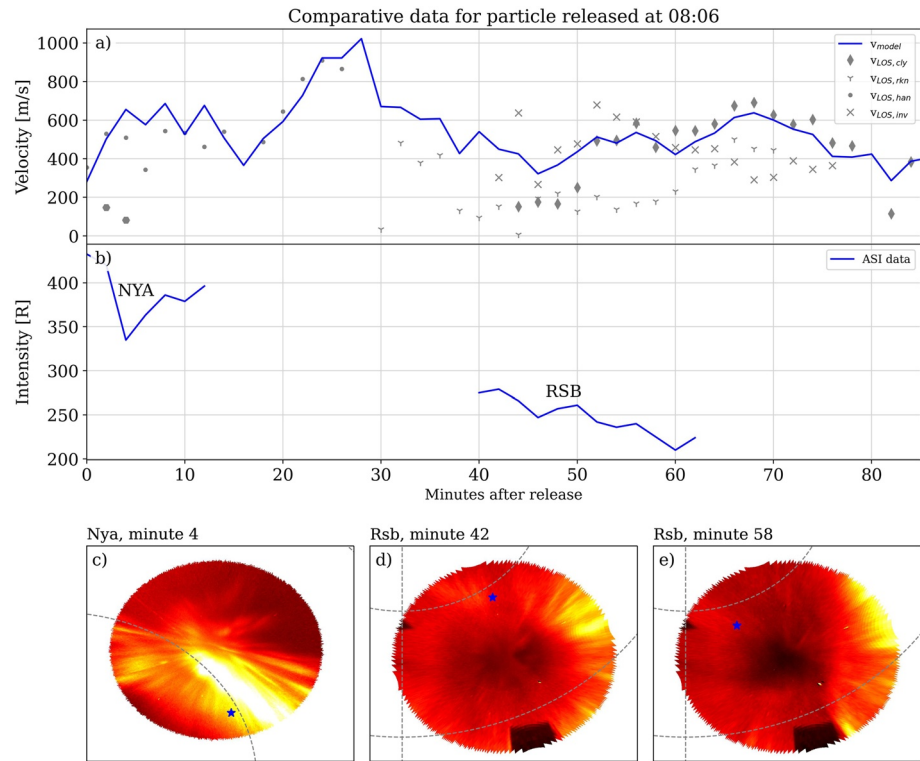
Figure 6. Same format as Figure 4, but for patch 3 released at 08:06 UT. The orientation of the cameras is as seen in Figure 3b.

determined by eye). It first enters the Clyde River radar FOV at minute 40 (08:46 UT) from the north-east, and at minute 50 (08:56 UT) it moves westward along beam 14, and at minute 62 (09:08 UT) it seems to have stopped moving within the radar's FOV. From this point on, we refer to this lack of movement with respect to the Clyde River FOV in the geographical reference frame as a stagnation. Around minute 70 (09:16 UT) the patch appears to start breaking up, that is, the backscatter power is decreasing and the areas where it is present is becoming more fragmented. This corresponds to a rapid decrease of backscatter power in Figure 7a, but also panels (h)–(j) show a clear reduction of backscatter area and magnitude. At minute 80 (09:26 UT) it appears that the remaining regions of high-power backscatter are of such small scale-lengths that they would no longer be considered a single polar cap patch, see panel (k). In Figure 7b we clearly see a strong flow away from the Clyde River radar, where the speed is especially high in the area where P3 starts to break up, indicating that enhanced flow contributes to its rapid separation into several small-scale regions of lower backscatter power than previously.

During minute 52 to 62, Clyde River beam 14 overlaps with the RSB FOV. Figure 6b shows that the airglow intensity decreased by 18 R during those 10 minutes, however the intensity measurements are uncertain due to low elevation angles, background emission and atmospheric absorption. Since it is possible, we calculate the backscatter half-life from the Clyde River radar. The total decrease in backscatter power for this period is 7.1 dB, corresponding to a half-life of 4.23 min. After the stagnation, between 68 and 78 min, the patch had a total decrease of 16.7 dB, or its half-life of backscatter power decreased to 1.80 min.

Figure 8 shows two images, with relative intensities, from RSB for (a) minute 44 (08:50 UT) and (b) minute 56 (09:00 UT), where the airglow patch corresponding to P3 has been outlined in blue, and the tracking position is shown as a blue star. We chose a location in the airglow patch (76.7407°N, −87.9282°W) and found that the new coordinate after 10 min was 76.9224°N, −102.3369°W. The airglow patch P3 moved with a velocity of 506.4 m/s. During this 10-min period it traveled along beam 8 and beam 9 in the Inuvik SuperDARN radar with a mean velocity of 520 m/s, while the SuperDARN convection model predicted a mean velocity of 424 m/s, giving a relative discrepancy of ≈19% between the model and LOS velocity, and ≈16% between the model and the ASI velocity.
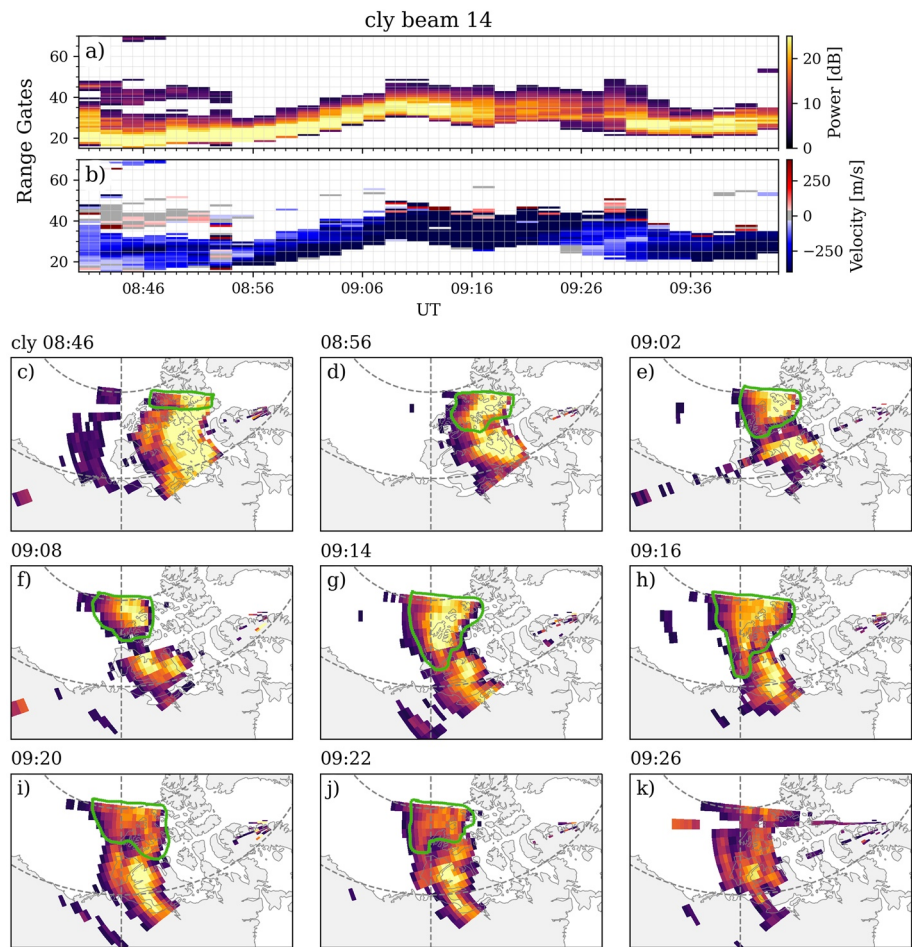
Figure 7. (a) backscatter power in beam 14 of the Clyde River SuperDARN radar. (b) shows the respective LOS velocity of the beam. (c)–(k) Clyde River fan plot of backscatter power for selected times. Measurements associated with P3 are outlined in green.

There is a difference between the SuperDARN convection velocity and the Clyde River LOS velocity for minute 60–78, as P3 moves along beam 14. The differences range from 25 to 78 m/s and the mean absolute error between the model and the LOS velocity is 52 m/s. This corresponds to a relative discrepancy of ≈9%. Table 1. summarizes the initial conditions during the release of P1, P2, and P3, in addition to their transit times.
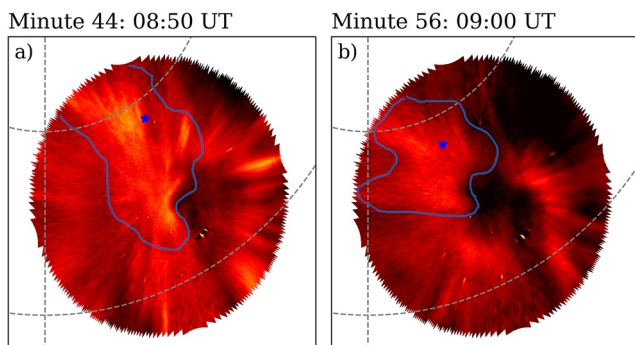

Figure 8. Images from Resolute Bay ASI where the airglow patch 3 is outlined in blue and the tracking position marked with a blue star for the times (a) 08:50 UT and (b) 09:00 UT.

5. Discussion

This paper presents the evolution of three polar cap patches from their creation on the dayside to their end of life on the nightside, where they either entered the auroral oval or decayed to the background density within the polar cap. The trajectories of the normal-density polar cap patches were estimated using SuperDARN convection maps.

The TOI is considered the source of the patches based on TEC data and ESR measurements. The southward IMF before the third patch supports the introduction of Solar EUV plasma into the polar cap, and subsequent formation of the patch due to transient flux transfer events on the dayside magnetopause (Lockwood & Carlson, 1992). During the creation of the two first patches the IMF was northward, which indicates lobe reconnection. Xing et al. (2012) and Wu et al. (2020) showed that a notable number of PMAF-occurrences

Table 1
Summary of Patch Properties

	P1	P2	P3
$t_{release}$ (UT)	07:06	07:18	08:06
$t_{transit}$ (minutes)	104	92	78
t_{exit} (UT)	08:58	09:04	N/A
$n_{initial}(m^{-3})$	1.14×10^{11}	1.48×10^{11}	2.92×10^{11}
$IMF_{initial}$ (x, y, z)	+,+,+	+,+,+	-,+,-
$CA_{initial}$ (degrees)	60	53	170

were in the IMF B_z = [-1,1]nT interval, while 41% and 31% (in the Southern Hemisphere) of PMAFs occurred under northward conditions, respectively. Wu et al. (2020) saw a similar occurrence rate for southward and northward IMF conditions and concluded that PMAFs were more likely to be plasma patches torn away from the auroral oval than direct foot points of reconnecting flux tubes. However, for P1 and P2 the TEC data show a clear transport of lower-latitude plasma toward the pole. Thus, we suggest that the lobe reconnection is the reason that P1 and P2 are less dense than P3, which is released during a PMAF with southward IMF. The changes in the convection velocity and the smaller angle between the ESR 32m FOV and the auroral oval are believed to be the cause of the reduced latitudinal extent of both the electron density signatures of P3 and the PMAF signatures seen in the temperatures in Figures 1c and 1d. In comparison, P1 has a more typical latitudinal extent for its signatures, while P2 is less dense than P1 and more stubby, which could be due to the more consistent IMF Bz seen at the time in Figure 1a.

5.1. Model Assessment

For the events presented in this work, SuperDARN provided good data coverage over the polar regions, allowing reasonable convection patterns to be determined in the regions where the patches were present. In addition, backscatter from the polar cap patches themselves were detected for a large part of their lifetimes, resulting in accurate measurements of velocities and direction. At times when the patches were in regions of sparse SuperDARN data coverage, their trajectory determination relied more heavily on the convection model, which introduces some uncertainties. Velocity shears and nonlinear convection velocities may influence trajectories. For example, P1 and P2 leave the polar cap at the same time, even though they were released 12 min apart. Therefore, it is essential to be mindful of the potential uncertainties that can arise from depending on the velocities of the convection model.

Other sources of error in the PCP trajectories are rapid spikes in the IMF clock angle that temporarily distort the convection pattern (Gjerloev et al., 2018), and the chosen release height assumption that determines the initial placement of the patch into the large-scale flow. The clock angle spikes seen right after 08:00 UT in Figure 1b were not of concern for us as the patch trajectories at the time were within an area of good data coverage, and the changes in the convection pattern had no major impact on the trajectories. However, the overall agreement between airglow patches seen in the optical measurements over NYA and RSB and the trajectories created between 06:50 and 08:30 UT are very good, indicating that the method works well with carefully determined initial release location. The events that were selected for the paper showed an especially good fit with the airglow patches.

An average of 583 SuperDARN data points were used in our tracking method, which was successful in tracking average-density polar cap patches, based on the coincident observations of high backscatter power and airglow patches. Comparably, in Oksavik et al. (2010) around 1,000 data points contributed to the convection maps when tracking two extreme electron density events. Additionally, the tracking method presented in this paper worked well when there were gaps in the optical data coverage as was seen for P3, that is, the tracking method connected the PMAF and high-density signatures seen on the dayside with the decreasing backscatter power seen in the Clyde River radar on the nightside. It is reasonable to assume that the tracking method could be used for any density structure in the ionosphere which drifts with the background convection.

Spicher et al. (2015) used SWARM data to measure a PCP at two distinct locations in the polar cap, in the dayside and in the nightside. The SWARM satellites had the initial "pearls-on-a-string"-formation, and the study provides a good example of how PCPs can be tracked over the polar cap outside of using SuperDARN and all-sky cameras. The tracking using SWARM is ideal when the satellite orbit is parallel to the PCP trajectory. Otherwise, it would be difficult to conclude if SWARM were measuring the same patch. Thus, we come back to the need for a general method of tracking PCPs that can tie together several types of instrument observations.

5.2. Transit Times and Intensification in the Nightside Auroral Boundary

P1 and P2 were found to have transit times of 104 and 92 min, respectively and both showed a pulsed speed as they traveled through the convection throat on their way to the nightside auroral oval. There are no clear

indications that the patch velocities differ from the background convection velocity, as reported by Thomas et al. (2015). However, the observation of auroral intensification close to the patches exit location at the end of the patches lifetime could indicate a relationship between the auroral intensifications and exiting patches.

At minute 94 for P1 and minute 82 for P2 (08:40 UT) the beginning of an auroral intensification in the nightside auroral oval could be seen in Video 1, followed by subsequent poleward moving, east-west aligned arcs. Poleward boundary intensifications (PBIs) have previously been associated with flow channels and airglow patches (e.g., Nishimura et al., 2013, 2014; Zesta et al., 2002). The fitted velocities vectors seen in Video S1 (see Supporting Information S1) close to P1 and P2 showed fast flows from 08:22 to 08:46 UT, which could potentially stem from an anti-sunward flow channel that triggered the PBI at 08:40 UT. P1 and P2 used 10 min to reach the nightside auroral oval after the first intensification occurred. At minute 96 a decrease in the velocity of P1 was seen, which lasted about 6 min. The same type of decrease in the velocity of P2 at minute 84 was seen, lasting around 10 min.

Nishimura et al. (2014) suggested that fast flow channels in the lobe that propagated toward the nightside plasma sheet could trigger local nightside reconnection, which appears as PBIs in the optical data. The trajectories of P1 and P2 do not align with the enhanced flow seen in the fitted velocity vectors in their last minutes, and their respective airglow patches are therefore not following the enhanced flow of the first PBI for their entire trajectory. Therefore, neither P1 nor P2 can be said to trigger the PBI. Data from ground magnetometers at Fort Smith and Fort Simpson showed no substorm signatures, suggesting that the PBIs did not trigger any local substorm reconnection on the nightside. Nishimura et al. (2013) reported an airglow patch with embedded polar cap arcs under substorm conditions, which went on to trigger a PBI as it reached the nightside auroral oval. P1 and P2 also appear to be embedded with small-scale aurora-arcs, yet under non-substorm conditions. There are few reports on airglow patches themselves triggering the occurrence of PBIs, but PBIs have been reported during non-substorm conditions previously (Lyons et al., 1999).

In addition to the PBI at 08:42 UT, several other PBIs were seen at 08:54, 09:00, 09:06, and 09:12 UT. Unfortunately, there are no SuperDARN measurements covering the region surrounding the trajectories of P1 and P2 during these times, so it was not possible to confirm that the PBIs were triggered by antisunward flow channels. Nor were there any 630.0 nm filtered ASI images during this period, so optical confirmation is also not possible. The observation of PBIs could be the ionospheric auroral footprint of bursty bulk flows setting up field aligned currents (Lyons et al., 1999) in the vicinity of P1 and P2 which could lead to nearby velocity shears. In addition, a scattering of most of the virtual particles released close in time to P1 and P2 (see gray dots in Video 1) indicates local velocity shears, which could be explained by P1 and P2 being within the nightside auroral oval.

McWilliams et al. (2000) found that plasma structures had different speeds depending on whether or not they existed within the footprint of an active reconnection region on the dayside. Some structures moved parallel or along the auroral oval boundary. It can therefore be understood that the changing size of the auroral oval itself influences the speed of a drifting plasma structure. In Video 1 the SSUSI model auroral oval boundary expands poleward as both P1 and P2 reach the edge, which would influence the convection flow in its vicinity, since plasma would only be able to pass through an area where reconnection is occurring. Previous studies have found that the auroral oval expands toward drifting airglow patches during active magnetic reconnection periods (e.g., Lorentzen et al., 2004). From the results presented in this paper it is reasonable to assume that reconnection occurs in the vicinity of P1 and P2 as they enter the auroral oval, however on such a scale that the magnetic disturbances occurring at ~250 km altitude are too small to propagate down to the ground magnetometer.

5.3. Airglow Variability

The airglow intensity shown in Figures 4b and 5b for P1 and P2, respectively, can both be seen to decrease as they move from the NYA FOV toward the RSB FOV. However, as the two patches move across the RSB FOV their intensities start to increase again at minute 72 and 64 for P1 and P2, respectively. During this time there is a lot of aurora activity in the nightside auroral oval, which can be seen in the Fort Smith and Fort Simpson images in Video 1, thus it is likely that the increase in intensity is due to either contributions from the small-scale arc-like structures embedded in the patches or from activity in the nightside aurora oval. As previously mentioned, the uncorrected intensity will be influenced by the elevation angles, the background emission as well as the atmospheric absorption. However, based on the activity seen in the RSB images during this time period the auroral activity seem to contribute to measurements to such a degree that it would not be possible to find an optical decay rate.

The Canadian High Arctic Ionospheric Network (CHAIN) (Jayachandran et al., 2009) digital ionospheric sounder at Cambridge Bay were operational during this time and provided NmF2- and HmF2-measurements. The NmF2-measurements from Cambridge Bay are presented in Figure S1 in Supporting Information S1, along with $N_{e,\text{max}}$-measurements from ESR 42 and 32m. The NmF2-measurements unfortunately cannot be used to derive a decay rate since it only provides a maximum electron density in the F2-region and no information about the density above this measurement. The CHAIN Eureka digital ionosonde was also operative at the time, but in extraordinary mode with a time cadence of 25 min. Therefore, it was not possible to compare the NmF2-measurements between the two digital ionosondes.

However, as seen in Figure S1 (see Supporting Information S1) there were three plateaus of NmF2-measurements which occurred at a time where we could expect the arrival of P1 and P2 based on the tracking. The two shaded gray regions are believed to correspond to the expected time of arrival of P1 and P2, respectively, while the blue shaded region could be an alternative time of arrival of P2. The HmF2-measurements of the two gray regions correspond to ~312 km for the first plateau and between 298 and 320 km for the second plateau. The blue region had HmF2-measurements between 304 and 316 km. The airglow seen in ASI images should be mapped to the bottom layer of the PCP, but given a HmF2-altitude of 300 km or more, the standard 230 km altitude mapping of the RSB images were probably not optimal for the airglow corresponding to P1 and P2. However, Cambridge Bay is located at the edge of the RSB FOV, and it does not necessarily mean that P1 and P2 had a constant HmF2 for all of RSB's FOV. Hosokawa et al. (2011) also showed that as the airglow patch traveled over the polar cap, the peak airglow height of the patch increased, due to the recombination in the bottom layers of the airglow patch. This means that the mapping altitude for a short sequence of ASI images containing airglow patches could be different based on the patch's bottom layer altitude, which makes it pragmatically more complicated. In addition, a downward motion of the patch from a downward component in the ExB-drift (Perry et al., 2013) could also influence the intensity due to change in the altitude-dependent recombination rate.

In Figure 6b the intensity is not seen to decrease when P3 is within the NYA FOV, but this is likely due to the PMAF taking up most of the NYA FOV while P3 lies within it. In contrast to P1 and P2, there is a clear decrease seen in the intensity while P3 moves within the RSB FOV. Unfortunately, the elevation angles are all between 20 and 30° and thus a robust linear optical decay rate is not possible to derive. However, in Figure 6b the intensity decreased by 51 R from minute 42 to 58, with an increase of 2.36° in elevation angle during the time. Thus, the Van Rhijn effects would be larger for minute 42 and the true intensity would therefore be stronger, this supports that there is an actual dimming of the airglow. Although, there is a general decrease of patch intensity seen within the RSB FOV, there are also fluctuating periods of intensifications, which could be due to the local changes at the P3-location, where panel (e) does show a dimmer airglow patch than panel (d). Gravity waves and vertical winds have been known to influence the 630.0 nm emission intensity in airglow patches (Valladares et al., 2015). Thus, these processes could potentially explain the fluctuating intensity that was observed in panel (b), which means a decay rate might be variable throughout a PCP's lifetime and could be sensitive to changes in the altitude of the patch's bottom layer.

5.4. Patch 3 and its End of Life

P3 was created after a longer period of Southward IMF where ESR measured more dense plasma compared to P1 and P2, see Figure 1a. P3's transit also differed from P1 and P2 as it never reached the nightside auroral oval, but instead underwent a complete decay within the polar cap.

Initially, P3 traveled within the convection throat with a steady velocity around 500 m/s for the first 20 min, before a rapid increase in velocity reaching 1000 m/s within the next 30 min. Considering Figure 1a a period of approximately 40 min of southward IMF is seen, starting a few minutes after 08:00 UT, which could result in increased dayside reconnection. The IMF was southward for P3 (northward for P1 and P2) and could explain the intense PMAF, and thus high flux transfer. This rapid reconnection rate could also be responsible for the enhanced flow seen in the convection throat (Ren et al., 2020), and thus the increase in the P3 velocity before minute 30.

Later, P3 moved within the LOS of beam 14 of Clyde River for almost 40 min before it appeared to completely disintegrate, that is, the backscatter power no longer showed its previous coherent signature and became indistinguishable from the ambient plasma. The observation provides a unique insight into what determines the decay of a polar cap patch. No significant indications in the solar wind measurements were present. However, convection

maps with their fitted velocities vectors indicate that P3 was close to a region of enhanced flows starting at minute 48 (08:54 UT). In the individual radars Clyde River, Rankin Inlet and Inuvik, the enhanced flows are sometimes structured as flow channels, but at other times they have a wider horizontal extent. As P3 entered the region of enhanced flow, the trajectory changed from moving straight toward magnetic midnight to a duskward direction. In addition, in Video 1 between minute 68 and 78, P3 and its 10 trailing gray dots appear to undergo a second rotation.

In the Kaktovik magnetometer (not shown), a tail loading phase starts at around 08:50 UT and shows a steady decreasing depression down to −100 nT until 09:34 UT before the onset of a −200 nT substorm occurs. In Figure 1a a turn from northward to southward IMF can be seen just before 08:00 UT, which could initiate the loading phase. One theory is that the loading phase could set up bursty bulk flows creating disturbances in the nightside convection which could lead to the enhanced flows and that these flows themselves could lead to the decay of P3. Rankin Inlet velocity fan plots indicate that there are regions in the vicinity of the P3 transit with flows in different directions which would lead to strong shears in the convection. Hosokawa et al. (2010) found that a polar cap patch with internal structures could be restructured into several smaller polar cap patches because of shears in the background convection and suggested it could also lead to a decrease in the density of polar cap patches due to potential changes in the vertical structure of the patches.

The gradient drift instability (GDI) has previously been seen to be relatively large in the trailing edge of a polar cap patch (Milan et al., 2002) and is also considered an important internal structuring mechanism of an airglow patch. As P3 underwent a rotation during its transit, this would indicate a new trailing edge with respect to the background convection. Assuming the GDI in the old trailing edge did not immediately stabilize, a new trailing edge would provide a larger portion of the polar cap patch border to be available for strong GDI, which would be free to propagate inwards and could potentially accelerate the density decay of P3, through redistribution of the plasma density and potential fragmentation from the main patch. Spectral width (not shown) related to the measurements from Clyde River beam 14 between 08:50 and 09:34 UT indicate a turbulent plasma, supporting a plasma with high instability and contributing to a rotation of the PCP.

Based on Clyde River backscatter power measurements in Figure 7a, P3 stagnates, compared to its previous movement, at minute 62 (09:08 UT). This stagnation appears to be a key step of the transit which results in a complete decay of the patch, by which we mean that it became indistinguishable from the background plasma. It should be mentioned that the strength of the radar backscatter signal is determined by several factors: the transmitted waves' orthogonality to the magnetic field (low aspect angles), irregularities in the plasma, and the amount of absorption along the propagation path (Greenwald et al., 1995; Ponomarenko et al., 2011), thus the backscatter power decrease could stem from different propagation condition rather than a decay in density, which would present a worse scattering target. Also, the SuperDARN power parameter is actually a signal-to-noise ratio (SNR), so the power values shown in Figure 7 are also dependent on the background noise level. However, during this interval the noise level measured by CLY remains reasonably constant, except for a small, temporary increase at 09:18 UT, thus the reduced SNR observed from 09:14 UT until 09:26 UT is not due to an increase in the noise level. However, in combination with ASI images, SuperDARN convection information and TEC maps from the World-wide GNSS Receiver Network (Rideout & Coster, 2006; Vierinen et al., 2016), seen in Figure S2 in Supporting Information S1, we believe that the observations do indicate a rapid decrease in density of the PCP. The TEC maps provided in Figure S2 in Supporting Information S1 are unfiltered, 1°×1° binned, 5-min averaged. The P3 airglow patch region is outlined in black in the figure, and the backscatter power region from Clyde River associated with P3 is outlined in gray. The data coverage within the outlined regions is somewhat scarce outside of panel (a), and thus the TEC maps are not suitable on their own to determine a decay in density, yet they support the hypothesis.

Fan plots show a rapid change in the Clyde River and Rankin Inlet LOS velocities, and the introduction of the enhanced flows mentioned above would create a big relative velocity difference in the ion drift and the neutral wind. This difference leads to increased frictional heating, which again leads to faster recombination, depleting the patch. Figure S3 in Supporting Information S1 shows neutral wind direction and magnitude at selected times of P3's trajectory, with neutral wind data from the Horizontal Wind Model 2014; Hedin et al., 1994; Hedin et al., 1996; Drob et al., 2015). Figure S3 in Supporting Information S1 suggests a substantial change in direction between the neutral wind and ion drift, due to a rotation of the ion velocity vector from southwest to northwest between minute 42 (08:48 UT) and minute 62 (09:08 UT). The model may not give a full representation of

the behavior of the neutral wind, as it is based on empirical evidence. However, the neutral wind response time has been reported to be both altitude dependent (from 45 min at 400 km to 1.5 hr at 200 km), as well as magnetic activity dependent (from 0.5 to 6.5 hr during active to quiet periods) (Deng et al., 2009; Kosch et al., 2001). Billett et al. (2019) showed that the neutral wind response time had a significant effect on the ion-neutral coupling, and thus energy transfer.

Hosokawa et al. (2011) studied the complete optical decay of an airglow patch during strong northward IMF conditions, and Q. H. Zhang et al. (2016) used TEC data to study the formation of a polar cap patch and its subsequent density decay during geomagnetic storm conditions and week northward IMF. Q. H. Zhang et al. (2016) saw that after the initial formation of the PCP the IMF turned from strong southward to weak northward conditions, which caused the trajectory of the patch to stagnate on the dayside, before its density decayed to the background levels. The decay in density of the PCP was suggested to be due to the effects stemming from the opposite directions of the ion drift and the neutral wind after the change in the IMF.

After the change of direction of P3 at minute 50 it took 12 min for the patch to stagnate, and 28 min to reach its end of life. This is within the reported neutral wind response time. Both Q. H. Zhang et al. (2016) and Hosokawa et al. (2011) present a PCP stagnating before complete density and optical decay, respectively. These three observations of complete decay of a PCP under different IMF and ionospheric conditions; weak northward with extreme density patch ($\approx$35 TECU) for Q. H. Zhang et al. (2016), strong northward ($\approx$4 nT) in Hosokawa et al. (2011), and southward ($\approx$2 nT) for minute 62 of P3, of ordinary electron density, suggest that the sudden change in the trajectory leads to a stagnation of the polar cap patch. Hence, stagnation becomes a key occurrence in deciding whether or not a polar cap patch would be able to exit the auroral oval on the nightside.

Ten minutes before the stagnation, the backscatter power had a half-life of 4.23 min. At minute 68 (09:14 UT) a rapid decay of Clyde River backscatter power is seen in Figure 7b and the half-life decreased to 1.80 min (minutes 68–74). Due to the lack of incoherent scatter radar measurements in the vicinity of P3 at minute 52 (78.42°N, 96.923°E) no relationship between electron density decay and backscatter power decay can be made. Instead, we compare the theoretical electron density decay rate, and therefore 630.0 nm emission decay rate, following the method described in Hosokawa et al. (2011). The MSIS-E−90 Atmosphere model (Hedin, 1991) gives the following values for neutral temperature [N$_2$] and [O$_2$] at 280 km: 975.2 K, 2.108E8 cm^{-3}, and 1.346E7 cm^{-3}. This produces a half-life of $\approx$34 min, which is substantially longer than the backscatter half-life of 4.23 min. It is reasonable to expect that the time constant from the model and the irregularities that create the backscatter echoes would be distinct. Additionally, as mentioned in Section 5.3, P3 had a decrease of 51 R between minute 42 to 58, which is a $\sim$20% decrease in intensity during the time period where the ion drift velocity vector rotates northwest.

Combined, this suggests that exponential decay, where we assume no production and neglect the divergence in the ion drift's influence on the decay rate, is not suitable for a PCP still in motion. Future investigations using incoherent scatter radar measurements at various stages of the PCP's lifetime are needed for a complete description of the decay rate. Nevertheless, the discussion indicates that the decay rate is not constant throughout the lifetime of a PCP.

The velocity measurements from Clyde River made it possible to compare the SuperDARN LOS and convection model velocity during the P3 transit. In Figure 6a during minute 60 and 78 the markers for Clyde River LOS velocity show a higher velocity than the convection model. The relative discrepancy between the Clyde River LOS and model velocity was found to be $\approx$ 9% or a mean absolute error of 52 m/s. This suggests an underestimation of the SuperDARN model convection velocity. Two possible contributors to this underestimation are (a) the SuperDARN velocity determination does not account for the ionospheric refractive index (Gillies et al., 2009), and (b) the SuperDARN analysis software performs median filtering and weighted averaging procedures on the LOS velocity measurements before determining the convection pattern.

An attempt at comparing the airglow patch velocity, the P3 transit velocity, and the Inuvik LOS velocity was done to see if the P3 transit velocity also showed an underestimation compared to the LOS velocity. Between minute 44 and 54 the airglow patch moved at a velocity of 506 m/s, and the Inuvik Radar had a mean velocity of 520 m/s, while the convection model velocity was 424 m/s giving a relative discrepancy of $\approx$16% and $\approx$19% for ASI velocity and Inuvik radar, respectively. This indicates that the SuperDARN convection velocity can be underestimated by almost 20% in some cases and is supported by previous reports of underestimation of the LOS

velocities (Gillies et al., 2009, 2010; Koustov et al., 2016; Ponomarenko et al., 2009) and the convection velocities (Fogg et al., 2020; Gao, 2012; Mori et al., 2012; Shepherd et al., 2002; Walach et al., 2022).

6. Conclusion

In this paper we have investigated three polar cap patch transits and their change in velocity, luminosity, and decay rates. The polar cap patches were of an average density and were created on the dayside from solar EUV dense-plasma and PMAFs, before they propagated over the polar cap. Two of the patches reached the nightside auroral oval, while the third decayed to the background plasma within the polar cap. We summarize our findings in the order they were discussed.

1. Given strong IMF By, which favors strong backscatter over the Canadian/Alaskan sector, the tracking of high-density plasma volumes in the ionosphere unites observations from different instruments that are not co-located.
2. Patches 1 and 2 transit in the convection throat and entered the nightside auroral oval. Their transit times were 104 and 92 min, respectively. In the last few minutes, of both patches, a decrease in velocity was seen as PBIs occurred in the vicinity of their exit point in the nightside polar cap.
3. Patch 3 reached its end of life after 78 min, as inferred from the radar backscatter power in Figure 7. A change in direction is observed due to enhanced flows, and the patch had a backscatter power half-life of 4.23 min. At minute 62 the patch appears to stagnate, and shortly after the half-life has decreased to 1.80 min, likely due to the increased frictional heating stemming from a relative velocity difference in ion drift and neutral wind. 16 minutes after stagnation, and 28 min after the change in transit direction, patch 3 were no longer distinguishable from the background.
4. A polar cap patch still in motion appears to have a variable decay rate.
5. The stagnation, and increased frictional heating (higher recombination rates), is theorized to be a major determinant to whether a polar cap patch will reach the nightside auroral oval or not.
6. The SuperDARN convection model underestimated the velocity with ≈19% and ≈16% compared to the Inuvik LOS velocity and RSB ASI airglow patch velocity.

Data Availability Statement

SuperDARN RAWACF data can be collected from the FRDR database (https://doi.org/10.20383/102.0448) and has been processed and analyzed using RST (https://doi.org/10.5281/ZENODO.5156752) and pydarn (https://doi.org/10.5281/zenodo.5762322) (SuperDARN Data Analysis Working Group et al., 2021). The Kp-index was provided by GFZ German Research Centre for Geosciences (Matzka, Bronkalla, et al., 2021; Matzka, Stolle, et al., 2021). The EISCAT data and DMSP SSIES data are available through the CEDAR Madrigal database (http://cedar.openmadrigal.org/) and the solar wind IMF data from ACE can be collected from https://cdaweb.gsfc.nasa.gov/index.html. The ASI data from UiO can be collected from http://tid.uio.no/plasma/aurora/ and THEMIS images are available from http://themis.igpp.ucla.edu/data_retrieval.shtml. The OMTI all-sky camera images are available from https://ergsc.isee.nagoya-u.ac.jp/index.shtml.en. The DMSP SSUSI data (product version V0105) was collected from https://ssusi.jhuapl.edu/data_products. MSIS values were collected from https://ccmc.gsfc.nasa.gov/modelweb/models/msis_vitmo.php. For the Supplementary Material data: The CHAIN data is available from http://chain.physics.unb.ca/chain/pages/data_download and the TEC maps are available from the CEDAR Madrigal database.

References

Billett, D. D., Wild, J. A., Grocott, A., Aruliah, A. L., Ronksley, A. M., Walach, M. T., & Lester, M. (2019). Spatially resolved neutral wind response times during high geomagnetic activity above Svalbard. *Journal of Geophysical Research: Space Physics*, 124(8), 6950–6960. https://doi.org/10.1029/2019JA026627

Carlson, H. C. (2012). Sharpening our thinking about polar cap ionospheric patch morphology, research, and mitigation techniques. *Radio Science*, 47(3). https://doi.org/10.1029/2011RS004946

Chisham, G., Lester, A. M., Milan, A. S. E., Freeman, A. M. P., Bristow, A. W. A., Grocott, A. A., et al. (2007). A decade of the super dual auroral radar network (SuperDARN): Scientific achievements, new techniques and future directions. *Surveys in Geophysics*, 28(1), 33–109. https://doi.org/10.1007/S10712-007-9017-8

Crowley, G. (1996). Critical review of ionospheric patches and blobs. *Review of Radio Science 1993–1996*, 619–648.

Deng, Y., Lu, G., Kwak, Y. S., Sutton, E., Forbes, J., & Solomon, S. (2009). Reversed ionospheric convections during the November 2004 storm: Impact on the upper atmosphere. *Journal of Geophysical Research*, 114(A7), 7313. https://doi.org/10.1029/2008JA013793

Drob, D. P., Emmert, J. T., Meriwether, J. W., Makela, J. J., Doornbos, E., Conde, M., et al. (2015). An update to the Horizontal Wind Model (HWM): The quiet time thermosphere. *Earth and Space Science*, *2*(7), 301–319. https://doi.org/10.1002/2014EA000089

Fogg, A. R., Lester, M., Yeoman, T. K., Burrell, A. G., Imber, S. M., Milan, S. E., et al. (2020). An improved estimation of SuperDARN Heppner-Maynard boundaries using AMPERE Data. *Journal of Geophysical Research: Space Physics*, *125*(5), e2019JA027218. https://doi.org/10.1029/2019JA027218

Foster, J. C., Coster, A. J., Erickson, P. J., Holt, J. M., Lind, F. D., Rideout, W., et al. (2005). Multiradar observations of the polar tongue of ionization. *Journal of Geophysical Research*, *110*(A9), 9–31. https://doi.org/10.1029/2004JA010928

Gao, Y. (2012). Comparing the cross polar cap potentials measured by SuperDARN and AMIE during saturation intervals. *Journal of Geophysical Research*, *117*(A8). https://doi.org/10.1029/2012JA017690

Gillies, R. G., Hussey, G. C., Sofko, G. J., McWilliams, K. A., Fiori, R. A., Ponomarenko, P., & St.-Maurice, J. P. (2009). Improvement of SuperDARN velocity measurements by estimating the index of refraction in the scattering region using interferometry. *Journal of Geophysical Research*, *114*(A7), 7305. https://doi.org/10.1029/2008JA013967

Gillies, R. G., Hussey, G. C., Sofko, G. J., Wright, D. M., & Davies, J. A. (2010). A comparison of EISCAT and SuperDARN F-region measurements with consideration of the refractive index in the scattering volume. *Journal of Geophysical Research*, *115*(A6). https://doi.org/10.1029/2009JA014694

Gjerloev, J. W., Waters, C. L., & Barnes, R. J. (2018). Deriving global convection maps from SuperDARN measurements. *Journal of Geophysical Research: Space Physics*, *123*(4), 2902–2915. https://doi.org/10.1002/2017JA024543

Goodwin, L. V., Iserhienrhien, B., Miles, D. M., Patra, S., Van Der Meeren, C., Buchert, S. C., et al. (2015). Swarm in situ observations of F region polar cap patches created by cusp precipitation. *Geophysical Research Letters*, *42*(4), 996–1003. https://doi.org/10.1002/2014GL062610

Greenwald, R. A., Baker, K. B., Dudeney, J. R., Pinnock, M., Jones, T. B., Thomas, E. C., et al. (1995). DARN/SuperDARN. *Space Science Reviews*, *71*(1), 761–796. https://doi.org/10.1007/BF00751350

Hays, P. B., Rusch, D. W., Roble, R. G., & Walker, J. C. G. (1978). The O I (6300 Å) airglow. *Reviews of Geophysics*, *16*(2), 225–232. https://doi.org/10.1029/RG016I002P00225

Hedin, A. E. (1991). Extension of the MSIS Thermosphere Model into the middle and lower atmosphere. *Journal of Geophysical Research*, *96*(A2), 1159–1172. https://doi.org/10.1029/90ja02125

Hedin, A. E., Buonsanto, M. J., Codrescu, M., Duboin, M. L., Fesen, C. G., Hagan, M. E., & Sipler, D. P. (1994). Solar activity variations in midlatitude thermospheric meridional winds. *Journal of Geophysical Research*, *99*(A9), 17601–17608. https://doi.org/10.1029/94JA01134

Hedin, A. E., Fleming, E. L., Manson, A. H., Schmidlin, F. J., Avery, S. K., Clark, R. R., et al. (1996). Empirical wind model for the upper, middle and lower atmosphere. *Journal of Atmospheric and Terrestrial Physics*, *58*(13), 1421–1447. https://doi.org/10.1016/0021-9169(95)00122-0

Hosokawa, K., Kashimoto, T., Suzuki, S., Shiokawa, K., Otsuka, Y., & Ogawa, T. (2009). Motion of polar cap patches: A statistical study with all-sky airglow imager at Resolute Bay, Canada. *Journal of Geophysical Research*, *114*(A4). https://doi.org/10.1029/2008JA014020

Hosokawa, K., Moen, J. I., Shiokawa, K., & Otsuka, Y. (2011). Decay of polar cap patch. *Journal of Geophysical Research*, *116*(5). https://doi.org/10.1029/2010JA016297

Hosokawa, K., St-Maurice, J. P., Sofko, G. J., Shiokawa, K., Otsuka, Y., & Ogawa, T. (2010). Reorganization of polar cap patches through shears in the background plasma convection. *Journal of Geophysical Research*, *115*(A1), 1303. https://doi.org/10.1029/2009JA014599

Hosokawa, K., Taguchi, S., & Ogawa, Y. (2016). Edge of polar cap patches. *Journal of Geophysical Research: Space Physics*, *121*(4), 3410–3420. https://doi.org/10.1002/2015JA021960

Hwang, K. J., Nishimura, Y., Coster, A. J., Gillies, R. G., Fear, R. C., Fuselier, S. A., et al. (2020). Sequential observations of flux transfer events, poleward-moving auroral forms, and polar cap patches. *Journal of Geophysical Research: Space Physics*, *125*(6), e2019JA027674. https://doi.org/10.1029/2019JA027674

Ivarsen, M. F., Jin, Y., Spicher, A., Miloch, W., & Clausen, L. B. (2021). The lifetimes of plasma structures at high latitudes. *Journal of Geophysical Research: Space Physics*, *126*(2), e2020JA028117. https://doi.org/10.1029/2020JA028117

Jayachandran, P. T., Langley, R. B., MacDougall, J. W., Mushini, S. C., Pokhotelov, D., Hamza, A. M., et al. (2009). Canadian high Arctic ionospheric network (CHAIN). *Radio Science*, *44*(1). https://doi.org/10.1029/2008RS004046

Jin, Y., Moen, J. I., & Miloch, W. J. (2014). GPS scintillation effects associated with polar cap patches and substorm auroral activity: Direct comparison. *Journal of Space Weather and Space Climate*, *4*, A23. https://doi.org/10.1051/SWSC/2014019

Kosch, M. J., Cierpka, K., Rietveld, M. T., Hagfors, T., & Schlegel, K. (2001). High-latitude ground-based observations of the thermospheric ion-drag time constant. *Geophysical Research Letters*, *28*(7), 1395–1398. https://doi.org/10.1029/2000GL012380

Koustov, A. V., Lavoie, D. B., & Varney, R. H. (2016). On the consistency of the SuperDARN radar velocity and E × B plasma drift. *Radio Science*, *51*(11), 1792–1805. https://doi.org/10.1002/2016RS006134

Lockwood, M., & Carlson, H. C. (1992). Production of polar cap electron density patches by transient magnetopause reconnection. *Geophysical Research Letters*, *19*(17), 1731–1734. https://doi.org/10.1029/92GL01993

Lockwood, M., Davies, J. A., Moen, J., Van Eyken, A. P., Oksavik, K., McCrea, I. W., & Lester, M. (2005). Motion of the dayside polar cap boundary during substorm cycles: II. Generation of poleward-moving events and polar cap patches by pulses in the magnetopause reconnection rate. *Annales Geophysicae*, *23*(11), 3513–3532. https://doi.org/10.5194/ANGEO-23-3513-2005

Lorentzen, D. A., Moen, J., Oksavik, K., Sigernes, F., Saito, Y., & Johnsen, M. G. (2010). In situ measurement of a newly created polar cap patch. *Journal of Geophysical Research*, *115*(12), 1–11. https://doi.org/10.1029/2010JA015710

Lorentzen, D. A., Shumilov, N., & Moen, J. (2004). Drifting airglow patches in relation to tail reconnection. *Geophysical Research Letters*, *31*(2). https://doi.org/10.1029/2003GL017785

Lyons, L. R., Nagai, T., Blanchard, G. T., Samson, J. C., Yamamoto, T., Mukai, T., et al. (1999). Association between Geotail plasma flows and auroral poleward boundary intensifications observed by CANOPUS photometers. *Journal of Geophysical Research*, *104*(A3), 4485–4500. https://doi.org/10.1029/1998JA900140

Matzka, J., Bronkalla, O., Tornow, K., Elger, K., & Stolle, C. (2021). Geomagnetic Kp index. V. 1.0. [dataset]. FZ Data Services. https://doi.org/10.5880/Kp.0001

Matzka, J., Stolle, C., Yamazaki, Y., Bronkalla, O., & Morschhauser, A. (2021). The geomagnetic Kp index and derived Indices of geomagnetic activity. *Space Weather*, *19*(5). https://doi.org/10.1029/2020SW002641

McWilliams, K. A., Yeoman, T. K., & Cowley, S. W. H. (2000). Two-dimensional electric field measurements in the ionospheric footprint of a flux transfer event. *Annales Geophysicae*, *18*(12), 1584–1598. https://doi.org/10.1007/S00585-001-1584-2

Milan, S. E., Lester, M., & Yeoman, T. K. (2002). HF radar polar patch formation revisited: Summer and winter variations in dayside plasma structuring. *Annales Geophysicae*, *20*(4), 487–499. https://doi.org/10.5194/ANGEO-20-487-2002

Moen, J., Oksavik, K., Alfonsi, L., Daabakk, Y., Romano, V., & Spogli, L. (2013). Space weather challenges of the polar cap ionosphere. *Journal of Space Weather and Space Climate*, *3*, A02. https://doi.org/10.1051/SWSC/2013025

Mori, D., Koustov, A. V., Jayachandran, P. T., & Nishitani, N. (2012). Resolute Bay CADI ionosonde drifts, PolarDARN HF velocities, and cross polar cap potential. *Radio Science*, *47*(3), 3003. https://doi.org/10.1029/2011RS004947

Nishimura, Y., Lyons, L. R., Shiokawa, K., Angelopoulos, V., Donovan, E. F., & Mende, S. B. (2013). Substorm onset and expansion phase intensification precursors seen in polar cap patches and arcs. *Journal of Geophysical Research: Space Physics*, *118*(5), 2034–2042. https://doi.org/10.1002/JGRA.50279

Nishimura, Y., Lyons, L. R., Zou, Y., Oksavik, K., Moen, J. I., Clausen, L. B., et al. (2014). Day-night coupling by a localized flow channel visualized by polar cap patch propagation. *Geophysical Research Letters*, *41*(11), 3701–3709. https://doi.org/10.1002/2014GL060301

Nishitani, N., Ruohoniemi, J. M., Lester, M., Baker, J. B. H., Koustov, A. V., Shepherd, S. G., et al. (2019). Review of the accomplishments of mid-latitude super dual auroral radar network (SuperDARN) HF radars. *Progress in Earth and Planetary Science*, *6*(1), 1–57. https://doi.org/10.1186/s40645-019-0270-5

Oksavik, K., Barth, V. L., Moen, J., & Lester, M. (2010). On the entry and transit of high-density plasma across the polar cap. *Journal of Geophysical Research*, *115*(A12). https://doi.org/10.1029/2010JA015817

Oksavik, K., Ruohoniemi, J. M., Greenwald, R. A., Baker, J. B. H., Moen, J., Carlson, H. C., et al. (2006). Observations of isolated polar cap patches by the European incoherent scatter (EISCAT) Svalbard and super dual auroral radar network (SuperDARN) Finland radars. *Journal of Geophysical Research*, *111*(A5). https://doi.org/10.1029/2005JA011400

Oksavik, K., Van Der Meeren, C., Lorentzen, D. A., Baddeley, L. J., & Moen, J. (2015). Scintillation and loss of signal lock from poleward moving auroral forms in the cusp ionosphere. *Journal of Geophysical Research: Space Physics*, *120*(10), 9161–9175. https://doi.org/10.1002/2015JA021528

Paxton, L. J., & Meng, C.-I. (1999). Auroral imaging and space-based optical remote sensing. *Johns Hopkins APL Technical Digest*, *20*(4), 556–569.

Paxton, L. J., Morrison, D., Zhang, Y., Kil, H., Wolven, B., Ogorzalek, B. S., et al. (2002). Validation of remote sensing products produced by the Special sensor ultraviolet Scanning imager (SSUSI): A far UV-imaging spectrograph on DMSP F-16. *Proceeding of SPIE*, *4485*, 338–348. https://doi.org/10.1117/12.454268

Paxton, L. J., & Zhang, Y. (2016). Far ultraviolet imaging of the Aurora. *Space Weather Fundamentals*, *11*, 213–244. https://doi.org/10.1201/9781315368474-14

Pedersen, T. R., Fejer, B. G., Doe, R. A., & Weber, E. J. (2000). An incoherent scatter radar technique for determining two-dimensional horizontal ionization structure in polar cap F region patches. *Journal of Geophysical Research*, *105*(A5), 10637–10655. https://doi.org/10.1029/1999JA000073

Perry, G. W., St.-Maurice, J. P., & Hosokawa, K. (2013). The interconnection between crosspolar cap convection and the luminosity of polar cap patches. *Journal of Geophysical Research: Space Physics*, *118*(11), 7306–7315. https://doi.org/10.1002/2013JA019196

Ponomarenko, P. V., Koustov, A. V., St.-Maurice, J. P., & Wiid, J. (2011). Monitoring the F-region peak electron density using HF backscatter interferometry. *Geophysical Research Letters*, *38*(21). https://doi.org/10.1029/2011GL049675

Ponomarenko, P. V., St-Maurice, J. P., Waters, C. L., Gillies, R. G., & Koustov, A. V. (2009). Refractive index effects on the scatter volume location and Doppler velocity estimates of ionospheric HF backscatter echoes. *Annales Geophysicae*, *27*(11), 4207–4219. https://doi.org/10.5194/ANGEO-27-4207-2009

Ren, J., Zou, S., Kendall, E., Coster, A., Sterne, K., & Ruohoniemi, M. (2020). Direct observations of a polar cap patch formation associated with dayside reconnection driven fast flow. *Journal of Geophysical Research: Space Physics*, *125*(4), e2019JA027745. https://doi.org/10.1029/2019JA027745

Rideout, W., & Coster, A. (2006). Automated GPS processing for global total electron content data. *GPS Solutions*, *10*(3), 219–228. https://doi.org/10.1007/S10291-006-0029-5/FIGURES/6

Rodger, A. S., Pinnock, M., Dudeney, J. R., Baker, K. B., & Greenwald, R. A. (1994). A new mechanism for polar patch formation. *Journal of Geophysical Research*, *99*(A4), 6425–6436. https://doi.org/10.1029/93JA01501

Ruohoniemi, J. M., & Baker, K. B. (1998). Large-scale imaging of high-latitude convection with super dual auroral radar network HF radar observations. *Journal of Geophysical Research*, *103*(A9), 20797–20811. https://doi.org/10.1029/98JA01288

Sandholt, P. E., Deehr, C. S., Egeland, A., Lybekk, B., Viereck, R., & Romick, G. J. (1986). Signatures in the dayside aurora of plasma transfer from the magnetosheath. *Journal of Geophysical Research*, *91*(A9), 10063–10079. https://doi.org/10.1029/JA091iA09p10063

Sandholt, P. E., Farrugia, C. J., & Denig, W. F. (2004). Detailed dayside auroral morphology as a function of local time for southeast IMF orientation: Implications for solar wind-magnetosphere coupling. *Annales Geophysicae*, *22*(10), 3537–3560. https://doi.org/10.5194/ANGEO-22-3537-2004

Sandholt, P. E., Farrugia, C. J., Moen, J., & Cowley, S. W. H. (1998). Dayside auroral configurations: Responses to southward and northward rotations of the interplanetary magnetic field. *Journal of Geophysical Research*, *103*(A9), 20279–20295. https://doi.org/10.1029/98JA01541

Shepherd, S. G., Greenwald, R. A., & Ruohoniemi, J. M. (2002). Cross polar cap potentials measured with Super Dual Auroral Radar Network during quasi-steady solar wind and interplanetary magnetic field conditions. *Journal of Geophysical Research*, *107*(A7), 1–5. https://doi.org/10.1029/2001JA000152

Shiokawa, K., Katoh, Y., Satoh, M., Ejiri, M. K., Ogawa, T., Nakamura, T., et al. (1999). Development of optical mesosphere thermosphere imagers (OMTI). *Earth Planets and Space*, *51*(7), 887–896. https://doi.org/10.1186/bf03353247

Shiokawa, K., Otsuka, Y., & Ogawa, T. (2009). Propagation characteristics of nighttime mesospheric and thermospheric waves observed by optical mesosphere thermosphere imagers at middle and low latitudes. *Earth Planets and Space*, *61*(4), 479–491. https://doi.org/10.1186/BF03353165

Southwood, D. J. (1987). The ionospheric signature of flux transfer events. *Journal of Geophysical Research*, *92*(A4), 3207–3213. https://doi.org/10.1029/JA092iA04p03207

Spicher, A., Cameron, T., Grono, E. M., Yakymenko, K. N., Buchert, S. C., Clausen, L. B., et al. (2015). Observation of polar cap patches and calculation of gradient drift instability growth times: A Swarm case study. *Geophysical Research Letters*, *42*(2), 201–206. https://doi.org/10.1002/2014GL062590

SuperDARN Data Analysis Working Group, Schmidt, M., Tholley, F., Martin, C., Billett, D., & Bland, E. (2021). SuperDARN/pydarn: PyDARN v2.2.1 [software]. Zenodo. https://doi.org/10.5281/ZENODO.5762322

SuperDARN Data Analysis Working Group, Schmidt, M., Bland, E., Thomas, E., Burrell, A., Coco, I., et al. (2021). SuperDARN/rst: RST 4.6 [software]. Zenodo. https://doi.org/10.5281/ZENODO.5156752

Thomas, E. G., Hosokawa, K., Sakai, J., Baker, J. B. H., Ruohoniemi, J. M., Taguchi, S., et al. (2015). Multi-instrument, high-resolution imaging of polar cap patch transportation. *Radio Science*, *50*(9), 904–915. https://doi.org/10.1002/2015RS005672

Valladares, C. E., Pedersen, T., & Sheehan, R. (2015). Polar cap patches observed during the magnetic storm of November 2003: Observations and modeling. *Annales Geophysicae*, *33*(9), 1117–1133. https://doi.org/10.5194/angeo-33-1117-2015

Van Der Meeren, C., Oksavik, K., Lorentzen, D., Moen, J. I., & Romano, V. (2014). GPS scintillation and irregularities at the front of an ionization tongue in the nightside polar ionosphere. *Journal of Geophysical Research: Space Physics*, *119*(10), 8624–8636. https://doi.org/10.1002/2014JA020114

Van Rhijn, P. J. (1919). On the brightness of the sky at night and the total amount of starlight. *The Astrophysical Journal*, *50*(31), 356. https://doi.org/10.1086/142513

Vierinen, J., Coster, A. J., Rideout, W. C., Erickson, P. J., & Norberg, J. (2016). Statistical framework for estimating GNSS bias. *Atmospheric Measurement Techniques*, *9*(3), 1303–1312. https://doi.org/10.5194/AMT-9-1303-2016

Walach, M. T., Grocott, A., Staples, F., & Thomas, E. G. (2022). Super dual auroral radar network expansion and its influence on the derived ionospheric convection pattern. *Journal of Geophysical Research: Space Physics*, *127*(2), e2021JA029559. https://doi.org/10.1029/2021JA029559

Walker, I. K., Moen, J., Kersley, L., & Lorentzen, D. A. (1999). On the possible role of cusp/cleft precipitation in the formation of polar-cap patches. *Annales Geophysicae*, *17*(10), 1298–1305. https://doi.org/10.1007/S00585-999-1298-4

Wannberg, G., Wolf, I., Vanhainen, L. G., Koskenniemi, K., Röttger, J., Postila, M., et al. (1997). The EISCAT Svalbard radar: A case study in modern incoherent scatter radar system design. *Radio Science*, *32*(6), 2283–2307. https://doi.org/10.1029/97RS01803

Weber, E. J., Buchau, J., Moore, J. G., Sharber, J. R., Livingston, R. C., Winningham, J. D., & Reinisch, B. W. (1984). F layer ionization patches in the polar cap. *Journal of Geophysical Research*, *89*(A3), 1683–1694. https://doi.org/10.1029/JA089IA03P01683

Wu, Y. J. J., Mende, S. B., & Frey, H. U. (2020). Simultaneous observations of poleward-moving auroral forms at the equatorward and poleward boundaries of the auroral oval in Antarctica. *Journal of Geophysical Research: Space Physics*, *125*(6), e2019JA027646. https://doi.org/10.1029/2019JA027646

Xing, Z. Y., Yang, H. G., Han, D. S., Wu, Z. S., Hu, Z. J., Zhang, Q. H., et al. (2012). Poleward moving auroral forms (PMAFs) observed at the Yellow river station: A statistical study of its dependence on the solar wind conditions. *Journal of Atmospheric and Solar-Terrestrial Physics*, *86*, 25–33. https://doi.org/10.1016/J.JASTP.2012.06.004

Zesta, E., Donovan, E., Lyons, L., Enno, G., Murphree, J. S., & Cogger, L. (2002). Two-dimensional structure of auroral poleward boundary intensifications. *Journal of Geophysical Research*, *107*(A11), 1–6. https://doi.org/10.1029/2001JA000260

Zhang, Q. H., Moen, J., Lockwood, M., McCrea, I., Zhang, B. C., McWilliams, K. A., et al. (2016). Polar cap patch transportation beyond the classic scenario. *Journal of Geophysical Research: Space Physics*, *121*(9), 9063–9074. https://doi.org/10.1002/2016JA022443

Zhang, Q. H., Zhang, B. C., Lockwood, M., Hu, H. Q., Moen, J., Ruohoniemi, J. M., et al. (2013). Direct observations of the evolution of polar cap ionization patches. *Science*, *340*(6127), 1597–1600. https://doi.org/10.1126/science.1231487

Zhang, Y., & Paxton, L. J. (2008). An empirical Kp-dependent global auroral model based on TIMED/GUVI FUV data. *Journal of Atmospheric and Solar-Terrestrial Physics*, *70*(8–9), 1231–1242. https://doi.org/10.1016/J.JASTP.2008.03.008

Zou, Y., Nishimura, Y., Lyons, L. R., Shiokawa, K., Donovan, E. F., Ruohoniemi, J. M., & Nishitani, N. (2015). Localized polar cap flow enhancement tracing using airglow patches: Statistical properties, IMF dependence, and contribution to polar cap convection. *Journal of Geophysical Research: Space Physics*, *120*(5), 4064–4078. https://doi.org/10.1002/2014JA020946